Biomaterials Science

PAPER

Check for updates

Hollow silver–gold alloy nanoparticles for enhanced photothermal/photodynamic synergetic therapy against bacterial infection and acceleration of wound healing†

Shanshan Lin,[a,b] Hui Chen,[a,b] Rui Wang,[a,b] Tongmeng Jiang,[a,b] Rui Wang*[a,b] and Fabiao Yu [ID] *[a,b]

Bacterial infection seriously restricts the wound healing process due to severe inflammation and delayed wound healing. Unfortunately, the overuse or improper use of antibiotics leads to the advent of multi-drug-resistant strains and intractable biofilms, severely affecting the therapeutic effect. Therefore, there is an urgent need to develop antibiotic-free strategies to accelerate the healing process of wounds with bacterial infection. Considering that single photothermal therapy (PTT) or photodynamic therapy (PDT) cannot fully meet the requirements of clinical sterilization and accelerating wound healing, herein, hollow silver–gold alloy nanoparticles immobilized with the photosensitizer molecule Ce6 (Ag@Au-Ce6 NPs) integrated with PTT and PDT are proposed for killing bacteria and accelerating wound healing. The photothermal conversion properties of Ag@Au-Ce6 NPs are obtained using an infrared thermal imager, and the generation of singlet oxygen ($^1O_2$) is verified with an $^1O_2$ fluorescent probe DCFH-DA. Manipulated by near-infrared laser triggered mild hyperthermia and limited ROS amount, Ag@Au-Ce6 NPs could effectively kill bacteria that are free and colonized on the surface of wounded skin, promoting epithelium migration and vascularization, further accelerating wound healing, which showed great promise for biomedical application.

1. Introduction

Bacterial infection exhibits an increasing threat to human health, especially chronic infected wounds that seriously influence people's lives.[1,2] Although most skin wounds could be healed within one or two weeks, bacteria infected skin injuries, especially full-thickness wounds, can cause severe pain, sepsis, or even death.[3] Bacterial infection seriously restricts the wound healing process due to severe inflammation and delayed wound healing.[4] To deal with the bacterial infection of skin wounds, various antibiotics such as penicillin, cephalothin and vancomycin have been widely applied in the clinic. Unfortunately, the overuse or improper use of antibiotics leads

to the advent of multidrug-resistant strains such as methicillin-resistant *Staphylococcus aureus* (MRSA) and intractable biofilms, which severely affects the therapeutic effect.[5,6] Therefore, there is an urgent need to develop antibiotic-free strategies to accelerate the healing process of wounds with bacterial infection.

Compared to the present method, nanomaterials based on gold and silver exhibit tremendous advantages in preventing wound infections and accelerating wound healing, which is mainly attributed to the tunable physicochemical properties.[7] The high surface–volume ratio of nanomaterials can enhance the contact and interaction with bacteria, triggering extensive antibacterial mechanisms and providing better therapeutic efficiency.[8] In addition, other factors such as size, shape and surface modification also influence the antibacterial activity of nanomaterials.[9] Among the nanomaterials-based therapeutic strategies, photothermal therapy (PTT) and photodynamic therapy (PDT) have aroused increasing attention due to their non-invasiveness, low toxicity and high controllability.[10–12] Generally, a photothermal conversion agent can transform light energy into heat energy under near-infrared laser illumination in the PTT process, thus generating local hyperthermia, which can accelerate blood circulation in the wound and

[a]Key Laboratory of Hainan Trauma and Disaster Rescue, The First Affiliated Hospital of Hainan Medical University, Hainan Medical University, Haikou 571199, China. E-mail: wangrui@hainmc.edu.cn, yufabiao@hainmc.edu.cn

[b]Engineering Research Center for Hainan Bio-Smart Materials and Bio-Medical Devices, Key Laboratory of Emergency and Trauma, Ministry of Education, Key Laboratory of Hainan Functional Materials and Molecular Imaging, College of Pharmacy, College of Emergency and Trauma, Hainan Medical University, Haikou 571199, China

further stimulate the proliferation of fibroblasts and reduce inflammation, thus shortening the wound healing process.[13] However, a strong laser can cause the local temperature to become too high, which will burn normal tissues during treatment.[14] PDT relies on photosensitizers for realizing the conversion from oxygen to reactive oxygen species (ROS) *via* energy transfer, which can destroy surrounding biomolecules through the oxidation process and kill bacteria.[15] However, a large amount of ROS is required to damage most bacteria through PDT alone, while excessive ROS often cause inflammation, fibrosis and even necrosis of normal tissues.[16] The single therapy cannot fully meet the requirements of clinical sterilization and wound healing (Scheme 1).

Therefore, combining the advantages of the two therapy modalities and adopting the PTT/PDT synergistic effect, that is, PTT with lower temperature and moderate PDT with limited ROS can more effectively promote wound healing while sterilizing.[17] The synergistic therapy increases the permeability of the bacterial membrane by increasing regional heat and the ROS generated through the PDT pathway can penetrate the bacterial cell wall with ease and further oxidize intracellular protein and disrupt the homeostasis of bacteria.[18,19]

To achieve the synergistic photothermal/photodynamic treatment of bacteria infected skin wounds, herein, hollow silver–gold alloy nanoparticles immobilized with the photosensitizer Ce6 (Ag@Au-Ce6 NPs) were proposed for killing bacteria and accelerating wound healing. The photothermal conversion properties of Ag@Au-Ce6 NPs were determined using an infrared thermal imager, and the generation of $^1O_2$ was verified with the $^1O_2$ fluorescent probe. Manipulated by the near-infrared region (NIR) laser triggered mild hyperthermia and limited ROS amount, Ag@Au-Ce6 NPs could effectively kill bacteria that are free and colonized on the surface of wounded skin, promoting epithelium migration and vascularization, further

accelerating wound healing, which showed great promise in biomedical applications.

## 2. Experimental section

2.1 Materials

Ascorbic acid (AA), silver nitrate (AgNO₃), HS-PEG-NH₂, gold(III) chloride trihydrate (HAuCl₄·3H₂O), *N*-hydroxysulfosuccinimide (NHS) and *N*-(3-dimethylaminopropyl)-*N*′-ethylcarbodiimide hydrochloride (EDC) were bought from Aladdin Biochemical Technology (Shanghai, China). Polyvinylpyrrolidone (PVP, K30) was purchased from Biorigin (Beijing, China). Female Balb/c mice purchased from Tianqin Biotechnology (Changsha, China) were fed adaptively for one week (12 hours light and 12 hours dark, SPF feeding environment). Ce6 was purchased from Macklin Biochemical (Shanghai, China). 2′,7′-Dichlorodihydrofluorescein diacetate (DCFH-DA) was purchased from Beijing Solarbio Science & Technology (Beijing, China). Live/dead bacterial viability and counting kits were purchased from Yuanye Bio-Technology (Shanghai, China). CCK-8 was purchased from MedChemExpress LLC (New Jersey, USA). Ultrapure water (18.25 MΩ cm) was used throughout this work using a WoTePu water purifier (Sichuan, China). All the reagents were stored under conditions indicated in the instructions and used directly without any purification.

2.2 Instruments

UV-vis spectra and optical density results were recorded using a multifunctional BioTeK SYNERGY H1 microplate reader. The OD_{260} results were studied using a Nanodrop one spectrophotometer. The size and potential of the nanoparticles were determined using a nanoparticle analyzer (HORIBA Scientific, SZ-100V2). Fluorescence imaging was performed using an Olympus FV3000 laser confocal microscope. The laser source devices (660 nm laser: a xenon light source with a 660 nm filter, PE300-T8. 808 nm: a laser diode controller with an 808 nm optical fiber collimator) used in the therapy were from Beijing China Education AuLight Technology (CEAuLight) Co., Ltd. The optical power density was determined using an optical power meter from CEAuLight. The external morphology and internal structure of cells and particles were characterized using a transmission electron microscope (HITACHI HT7800) and scanning electron microscope (HITACHI SU8100). The temperature was monitored by FLIR infrared thermal imager (E53).

2.3 Preparation of silver nanoparticles and hollow Ag@Au nanoparticles

The preparation of silver nanoparticles was carried out based on the previous literature with slight modifications. All glassware were soaked in freshly prepared aqua regia before use and washed with ultrapure water. 85 mg of PVP and 85 mg of AgNO₃ were added to 20 mL of water and dissolved by stirring. After this, AgCl colloids were prepared by adding 200 μL NaOH (5 M) and stirring in the dark for 15 min. 60 mL of 50 mM
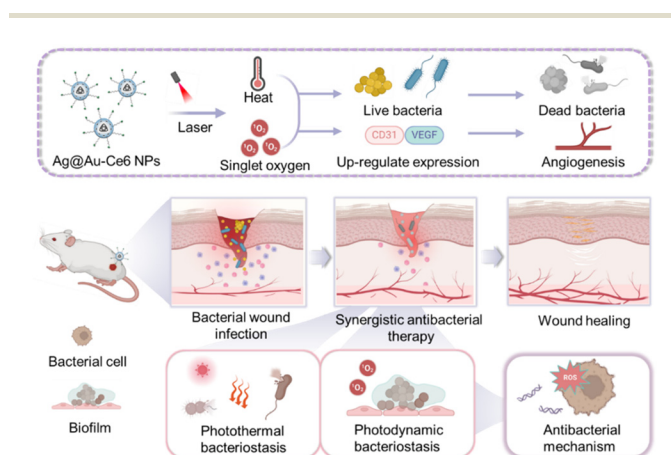
Scheme 1 Schematic illustration of Ag@Au-Ce6 NPs for bacterial eradication and wound healing acceleration. The constructed Ag@Au-Ce6 NPs eliminate planktonic and biofilm bacteria through synergistic photothermal and photodynamic effects, and induce the up-regulation of VEGF and CD31 to promote better wound healing. The illustration was created with the help of BioRender.com.

ascorbic acid solution was prepared and 6.9 mL of sodium hydroxide solution (0.5 M) was added. The fresh silver chloride colloid prepared above was added dropwise under the uniform stirring of a magnetic stirrer. PVP-coated silver nanospheres were prepared by stirring for 2 h in the dark. 12.5 mL of PVP-coated silver nanospheres prepared above were rinsed three times with ultrapure water and then concentrated into 1 mg mL^{-1} PVP aqueous solution. After the mixed solution boiled, the temperature was adjusted to keep the solution in a slightly boiling state and maintained for 10 minutes. Subsequently, a high-precision syringe pump was used to add the chloroauric acid solution (0.4 mM) at a flow velocity of 0.75 mL h^{-1}. The color change of the solution in the three-neck flask was observed, and the UV-vis spectra of solution samples were recorded. When the maximum absorption wavelength was close to 740 nm, the operation of the syringe pump was stopped. The solution was heated until the color reached a stable state. The flask was cooled by placing it in an ice bath, and then ammonia solution was added to dissolve the resulting silver chloride precipitate. Finally, the nanoparticles were washed three times, and finally suspended in 12.5 mL ultrapure water.

2.4   Fabrication of Ag@Au-Ce6 NPs

HS-PEG-NH$_2$ activated with TCEP was added to 1 mL of 1 nM hollow Ag@Au NPs, stirring at a speed of 260 rpm for 12 hours. After sonication of Ce6 (0.036 mg) and EDC (0.288 mg) for 30 min, NHS (0.144 mg) was added and vigorously shaken for 2 h. The Ce6 solution activated by the above process was added to the colloidal solution slowly dropwise and stirred at low speed for 24 h, keeping out of light. The excess free Ce6 was washed off by centrifugation three times to obtain the final Ag@Au-Ce6 NPs. Characterization was performed through UV-vis, DLS and TEM.

2.5   Photothermal performance assessment

The Ag@Au-Ce6 NPs solution was placed in the EP tube with different concentrations (0.25, 0.5, 1, and 2 nM). The temperature variation of the solution was recorded every 30 s by an infrared imaging device with a laser power density of 800 mW cm^{-2}. In addition, an 808 nm laser with different power densities (400, 800, and 1200 mW cm^{-2}) was irradiated for the same concentration of solution (1 nM), and the temperature was recorded (30 s interval). The calculation of the photothermal conversion coefficient is dependent on the 1 nM solution. The temperature of the solution was monitored for 5 min under 800 mW cm^{-2} irradiation and 15 min after the cessation of irradiation. The above process was repeated for five cycles during the thermal stability tests.

2.6   Singlet oxygen generation ability of Ag@Au-Ce6 NPs

The commercially available SOSG probe was dissolved in methanol to prepare stock solution with 1 mM concentration. The final concentration of detecting the singlet oxygen generation capacity was 1 μM. The mixed solution of the SOSG probe and Ag@Au-Ce6 NPs was added to a quartz cup and irra-

diated with a laser power of 200 mW cm^{-2} (660 nm). The intensity of the fluorescence signal was detected at 1, 2, 5, 10, 15, and 20 min, respectively. The excitation wavelength is 488 nm, and the collected emission wavelength range is 520–700 nm.

2.7   Bacterial strains and bacterial culture

Staphylococcus aureus (*S. aureus*, ATCC 25923) and *Escherichia coli* (*E. coli*, ATCC 25922) were purchased from the Guangdong Microbial Culture Collection Center (GDMCC). Freeze-dried bacterial strains were inoculated and transferred to LB agar plates after resuscitation using the LB medium. Subsequently, a single colony was selected and cultured in an LB liquid medium. After shaking for 10 h at 220 rpm, the colony grew to the logarithmic growth phase of bacteria. The bacteria were centrifuged to remove the upper medium, rinsed three times with sterile PBS, and stored at 4 °C.

2.8   *In vitro* antibacterial assays

In vitro antibacterial experiments were carried out in 96-well plates. 25 μL PBS and Ag@Au-Ce6 NPs (2.5, 1.25, 0.625, and 0.3125 nM) were added to the well containing 100 μL bacteria (10^7 CFU per mL). In addition, blank (LB medium) was set and incubated at 37 °C for 30 min under the same conditions. The experimental groups of bacterial solution which contained Ag@Au-Ce6 NPs were irradiated with an 808 nm (800 mW cm^{-2}, 5 min) and a 660 nm laser (200 mW cm^{-2}, 5 min), respectively. Then, the solution in the 96-well plate was diluted with the LB broth medium. After static culture for 24 h, the turbidity of the solution in the treated glass was observed and the OD$_{600}$ results were measured to determine the minimum inhibitory concentration (MIC).

The live/dead bacterial staining assay was utilized to evaluate the antibacterial effect *in vitro*. The bacterial suspensions were divided into four groups: PBS, PBS + laser (808 nm, 5 min + 660 nm, 5 min), Ag@Au-Ce6 NPs, and Ag@Au-Ce6 NPs + laser (808 nm, 5 min + 660 nm, 5 min). After treatment, SYTO 9 (E$_x$: 488 nm, E$_m$: 510–550 nm) and PI (E$_x$: 561 nm, E$_m$: 617–667 nm) dyes were added for 10 min in the dark, and the mixture was maintained at 25 °C in a constant temperature oscillator, shaking at a speed of 200 rpm. After centrifugation three times at 3500 rpm for 5 min, the bacterial precipitation was resuspended in sterile saline. The resuspended bacteria droplets were added to glass slides for observation under a confocal laser scanning microscope (CLSM).

The synergistic antibacterial performance of Ag@Au-Ce6 NPs was verified by colony formation experiments. Eight groups were formed, namely PBS, PBS + laser (808 nm, 5 min + 660 nm, 5 min), Ag@Au NPs, Ag@Au NPs + laser (808 nm, 5 min), Ce6, Ce6 + laser (808 nm, 5 min), Ag@Au-Ce6 NPs, and Ag@Au-Ce6 NPs + laser (808 nm, 5 min + 660 nm, 5 min). Ag@Au NPs and free Ce6 were used at concentrations corresponding to the MIC. The bacterial suspensions, PBS or experimental nanomaterial were added to the 96-well plate, co-incubated at 37 °C for 30 min. After four groups underwent irradiation, the bacterial suspensions were diluted and uni-

formly spread onto the agar plate. The total number of colony forming units was counted after incubation for 24 h at 37 °C.

2.9 Preparation of bacterial biofilms

Bacterial suspension in logarithmic phase was centrifuged and resuspended in sterile PBS. Subsequently, the culture was diluted with the LB broth medium to a final concentration of 10^7 CFU per mL. The bacteria were cultured in an incubator for 24 h without shaking, and the medium was gently replaced with the fresh LB medium after 12 h of incubation.

2.10 Inhibition of biofilm formation assay

100 μL of *S. aureus* suspensions (10^7 CFU per mL) were added to a 96-well plate containing 25 μL 1.25 nM Ag@Au-Ce6 NPs, and then mixed thoroughly at 37 °C in the dark for 30 min. Then the bacteria were irradiated with an 808 nm laser at 0.8 W cm^{-2} and a 660 nm laser at 200 mW cm^{-2} for 5, 3, 1, and 0 min, respectively. PBS treated *S. aureus* was used as a negative control group, while the sole LB broth medium group was used as a blank. The bacterial culture was transferred and cultured in a 24-well plate at 37 °C for another 24 h to examine the formation of the biofilm.

2.11 Inhibition of the formed biofilm assay

200 μL of *S. aureus* in the logarithmic stage were cultured in 96-well LB culture plates at a concentration of 10^7 CFU per mL, and biofilms were formed at the bottom of the plates after 24 h of static culture. After discarding the LB medium, sterile PBS was gently added twice for cleaning the remaining planktonic bacteria. Then, different concentrations of Ag@Au-Ce6 NPs (0.125, 0.25, 0.5, and 1 nM) and sterile PBS were added to bacteria for 30 min, respectively. Then the biofilm samples were irradiated with 200 mW cm^{-2}, 660 nm laser for 5 min and 0.8 W cm^{-2}, 808 nm laser for 5 min. The biofilms were fully separated from the well plate by ultrasonication and then were sampled, diluted, and added to the 48-well plate, and incubated for 24 h. When the stable biofilm was formed, it was stained with crystal violet. The absorbance at 590 nm (OD$_{590}$) was tested using a microplate reader to further verify the antibacterial effect on the formed biofilm. In addition, the treated biofilm suspension was diluted with LB and then added to confocal Petri dishes. After culturing for 24 hours, the upper layer of the medium was gently sucked off and the dye solution (SYTO 9, E$_x$: 488 nm, E$_m$: 510–550 nm) was added. After incubation for 8 min at room temperature, protecting from light, the dye solution was discarded and sterile PBS was added. The biofilm thickness was measured in the *Z* axis through CLSM.

2.12 Detecting intracellular ROS

The production of ROS in bacteria was imaged using the classical ROS fluorescent probe DCFH-DA. Bacterial suspensions were incubated with PBS, Ag@Au-Ce6 NPs with and without laser irradiation (808 nm, 5 min + 660 nm, 5 min). DCFH-DA was added with a final concentration of 20 μM and incubated at 37 °C for 30 min at 200 rpm. This was followed by centrifugation and washing three times before being resuspended in

PBS and fixed on glass slides with glycerol gelatin sealing solution for observation by CLSM.

2.13 TEM and SEM sample preparation and observation of bacteria

The bacteria in the logarithmic growth phase were centrifuged, rinsed and resuspended in sterile PBS to a final concentration of 2×10^9 CFU per mL. PBS, Ag@Au NPs, Ce6, and Ag@Au-Ce6 NPs were added to the four groups, respectively. The PBS group without any laser irradiation was used as a control, while the latter three groups were irradiated with an 808 nm laser for 5 min, a 660 nm laser for 5 min, and an 808 nm laser for 5 min + 660 nm for 5 min, respectively. Until the treatment was completed, the bacterial cells were centrifuged at 4000 rpm for 10 minutes then an electron microscope fixative (2.5% glutaraldehyde) was added to fix the structure and morphology of bacteria. Subsequently, the bacteria were resuspended in phosphate buffer. The above bacterial samples were then fixed with 1% osmic acid at room temperature in the dark for 2 h, and further rinsed with PB buffer 3 times. The samples were further dehydrated in 30%–50%–70%–80%–95%–100%–100% gradient concentrations of alcohol at room temperature for 20 min each time, followed by 100% acetone twice for 15 min each time. The bacterial samples were placed in an embedding plate containing the embedding agent and incubated at 37 °C overnight and an additional 48 h at 60 °C, the resin blocks were removed and sectioned with an ultra-thin microtome (thickness of 60 to 80 nm). The pieces were then collected with a copper mesh and stained with 2% uranyl acetate saturated alcohol solution and 2.6% lead citrate for 8 min, respectively. The final dried copper meshes were observed using a transmission electron microscope.

The initially fixed bacteria were repeatedly washed with 0.1 M PB three times before post-fixing with 1% osmic acid for 2 h. After rinsing with PB buffer, the above samples were sequentially dehydrated at room temperature over a gradient concentration of 30%–50%–70%–80%–95%–100%–100% alcohol for 20 minutes each, followed by isoamyl peracetate twice for 15 min each. The samples were dried in the critical point dryer, and then treated with the Au sputter for 30 s before observation under a scanning electron microscope.

2.14 Nucleic acid release assay

Nucleic acid leakage was evaluated by measuring the UV-vis absorbance of the bacterial suspension supernatant (260 nm). After the bacterial solution was diluted to 10^7 CFU per mL, PBS, Ag@Au NPs, Ce6, and Ag@Au-Ce6 NPs were added with and without laser irradiation. Afterward, the treated products were centrifuged, and the supernatant was collected and filtered through a 0.22 μm filter membrane. The results of nucleic acid leakage were determined by OD$_{260}$ with a Nanodrop one spectrophotometer.

2.15 Detection of the bacterial outer membrane potential

S. aureus and *E. coli* culture grown to the logarithmic growth phase was centrifuged and rinsed with PBS. And then the bac-

terial culture was resuspended at a concentration of 2×10^7 CFU per mL in 5 mM preconfigured HEPES buffer containing 100 mM potassium chloride and 20 mM glucose. 50 μL bacterial solution and 0.8 mM DiSC3(5) fluorescent dye were added to the specialized black 96-well plate. The plate was immediately placed in a microplate reader for fluorescence detection (E_x/E_m: 620 nm/670 nm), and incubated at 37 °C. The fluorescence value was read every 10 minutes until the fluorescence intensity gradually stabilized after 1 h. Subsequently, the bacterial suspensions in 96-well plates were treated with the different reagents of PBS, HEPES buffer, 0.5% Triton solution, Ag@Au-Ce6 NPs and Ag@Au-Ce6 NPs, respectively, which were further irradiated with laser (808 nm, 5 min + 660 nm, 5 min). The variation of fluorescence was monitored continuously at 10 min intervals. The time-dependent fluorescence signals were plotted at the end of the experiment.

2.16 *In vivo* antibacterial assays

All animal procedures were performed in accordance with the Guidelines for Care and Use of Laboratory Animals of Hainan Medical University and approved by the Animal Ethics Committee of Hainan Medical University. *In vivo* antibacterial experiments were conducted on the bacterial infection wound model in mice. Mice (18–22 g, 8 weeks) were randomly divided into 6 groups (n = 3): blank (no bacterial infection), PBS (bacterial inoculation, PBS treated), Ag@Au NPs + laser (bacterial inoculation, 808 nm, 5 min), Ce6 + laser (bacterial inoculation, 660 nm, 5 min), Ag@Au-Ce6 NPs (bacterial inoculation, without laser irradiation), and Ag@Au-Ce6 NPs + laser (bacterial inoculation, 808 nm, 5 min + 660 nm, 5 min). On day 0, 0.6% sodium isopentyl barbital (0.12 mL per 10 g) was used for intraperitoneal anesthesia, and full-thickness wounds were formed on the right back of the mice above the hip with a hole perforator (diameter: 8 mm). 50 μL of bacterial suspension (2×10^7 CFU per mL) was dropped onto the wounds of the mice except the blank group. Scheduled treatments of different groups were carried out on the first and the third day. On days 0, 2, 4, 6 and 8, the mice were photographed and their weights were recorded. On day 8, blood samples were collected from the posterior orbital vein in mice. On the 8th day, the mice were anesthetized and the wounded skin tissue was collected. The healing rate of the wound was calculated as follows: healing rate = $(1 - day_x$ wound area/day_0 wound area$) \times 100\%$. Skin tissues were fully vortexed in sterile normal saline to release the bacteria and the bacteria-containing solution was sampled on agar plates (37 °C, 24 h). The vital organs of the mice were harvested after euthanasia. HE staining, Masson staining and immunohistochemical staining (VEGF, ab51745 and CD31, ab124432) were performed on the collected skin tissues, and HE staining was performed on the main organs.

2.17 Biological safety evaluation

The biotoxicity of the constructed Ag@Au-Ce6 NPs was evaluated. The cytotoxicity test was performed as follows. NIH-3T3 cells, HUVEC cells, and HACAT cells were cultured in the special medium, respectively. The cells were passaged three

times to achieve optimal conditions after resuscitation. Then, different concentrations of nanoparticles (0.25, 0.5, 1, 2, and 4 nM) were added, and 1×10^4 of the cells were incubated for 24 h (37 °C, 5% CO₂). 10 μL of the CCK-8 reagent was added per well to detect cell viability to evaluate the dark toxicity of Ag@Au-Ce6 NPs on cells. The absorbance at 450 nm (A) was read using a microplate reader, and cell viability was calculated according to the following formula: cell viability = $(A - A_{blank})/(A_{control} - A_{blank}) \times 100\%$.

2.18 Statistical analysis

Data were presented as mean ± standard deviation (SD). Statistical analysis was performed by Graphpad prism 8. One-way analysis of variance (ANOVA) followed by the Tukey test was utilized for multiple comparisons. $P < 0.05$ indicates that a significant difference exists.

3. Results and discussion

3.1 Preparation and characterization of Ag@Au-Ce6 NPs

The preparation process of Ag@Au-Ce6 NPs is shown in Fig. 1A.[20,21] Ag@Au NPs were synthesized by the galvanic replacement reaction of HAuCl₄ in Ag NP solution.[22] Then the photosensitizer Ce6 was connected with the outer HS-PEG-NH₂ shell of Ag@Au NPs by the amide condensation reaction to prepare Ag@Au-Ce6 NPs. During the preparation process of Ag@Au NPs, the appearance of the solution changed from yellow to blue with the increasing addition of HAuCl₄ in Fig. 1B. Upon the addition of 22 mL, the colloidal solution turned blue indicating the preliminary synthesis of Ag@Au NPs. And the corresponding maximum UV-vis absorption peak located at 740 nm in Fig. 1D. TEM images indicated that the prepared Ag@Au NPs and Ag@Au-Ce6 NPs had hollow structures and uniform sizes (Fig. 1C). After immobilizing Ce6, DLS data indicated a slight increase of the probe size and more negative charge for the zeta potential owing to the negative charge of the carboxyl group in Ce6 (Fig. 1E and F), which further affirmed the successful construction of Ag@Au-Ce6 NPs.

The EDS elemental analysis plots in Fig. 1G showed the uniform distribution of Ag, Au, and N elements confirming the composition of Au–Ag alloy nanoparticles and Ce6 conjugation. The concentration of nanoparticles was estimated by the amount of silver element added to the initial system and the diameter of the synthesized silver nanoparticles. The initial concentration of Ag NPs was calculated to be about 1 nM.

3.2 Assessment of photodynamic and photothermal properties

Ce6 has strong absorption peaks at 400 nm and 670 nm. After being immobilized on the surface of Ag@Au NPs, two peaks at 410 nm and 675 nm could be observed with a slight red shift compared with that of Ce6, indicating successful conjugation as presented in Fig. 2A. In order to calculate the encapsulation efficiency of Ce6 on Ag@Au-Ce6 NPs, the calibration curve between absorbance values at 400 nm and the concentration
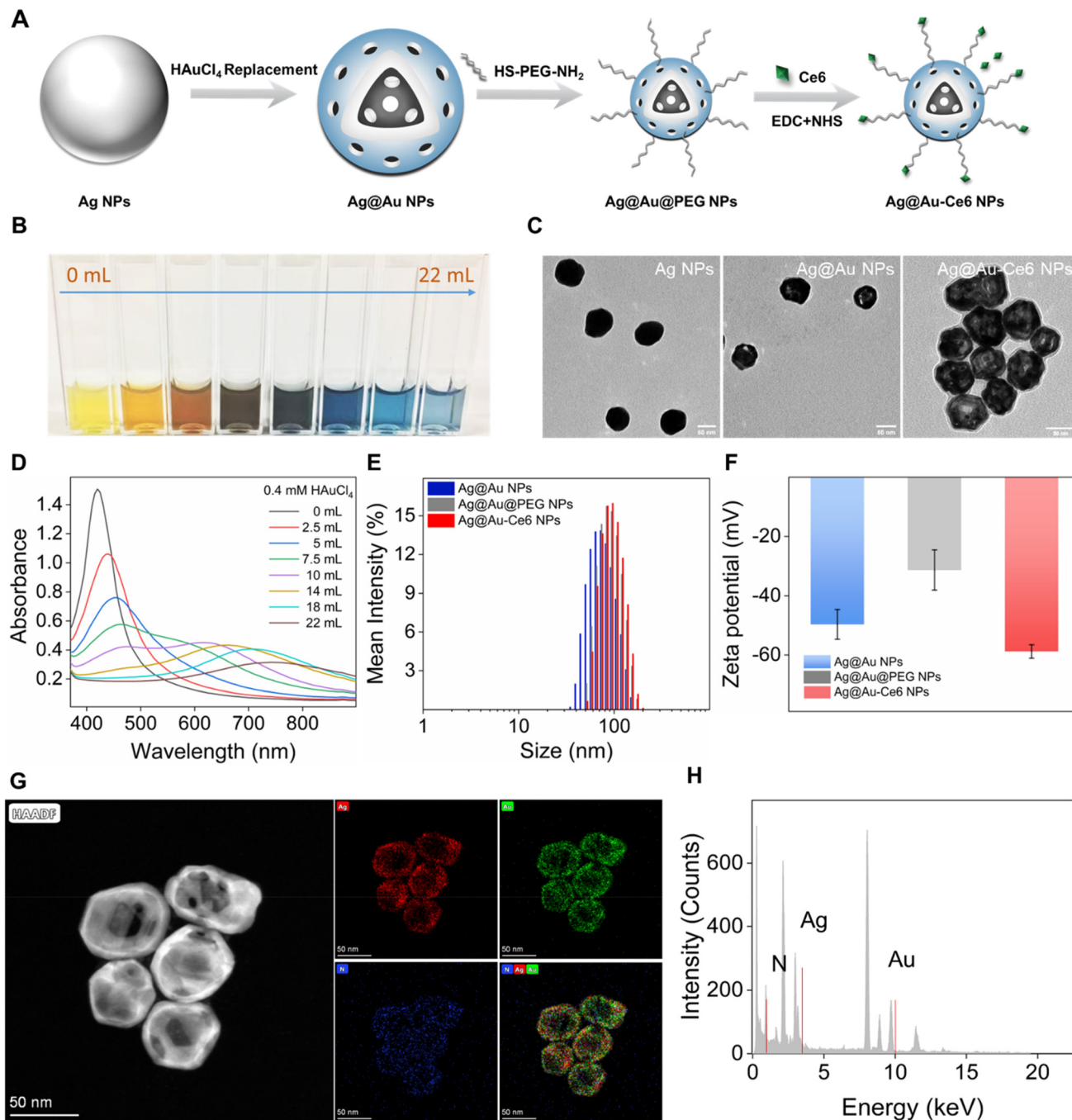
Fig. 1 The preparation and characterization of Ag@Au-Ce6 NPs. (A) Schematic illustration of the preparation of Ag@Au-Ce6 NPs. (B) The photograph shows the color changes of the colloid solution with the addition volume of HAuCl$_4$ (0.4 mM) from 0 mL to 22 mL. (C) TEM images of Ag NPs, Ag@Au NPs and Ag@Au-Ce6 NPs, scale bar: 50 nm. (D) UV-vis absorption spectra of Ag@Au NPs prepared with increasing volume of HAuCl$_4$. The hydrodynamic size distribution (E) and zeta potential (F) of Ag NPs, Ag@Au NPs and Ag@Au-Ce6 NPs. (G) and (H) The EDS mapping of the Ag@Au NPs (Au: green, Ag: red, N: blue) and the corresponding high-resolution STEM image.

of Ce6 was plotted in the range of 0–100 μg mL^{-1} (Fig. 2B). The encapsulation efficiency was calculated to be 54.9% according to the content of Ce6 in the supernatant and the encapsulation content.[23] The generation efficacy of $^1O_2$ significantly affects the PDT performance. To evaluate the $^1O_2$ production of Ag@Au-Ce6 NPs under 660 nm laser irradiation, the commercial $^1O_2$ fluorescent probe SOSG was utilized to test the fluo-

rescence spectra under 488 nm excitation, which was insensitive to hydroxyl radicals or superoxide. In the presence of $^1O_2$, green fluorescence could be detected and the fluorescence intensity at 528 nm rapidly increased within 20 min under 660 nm laser irradiation, demonstrating the continuous generation of $^1O_2$ from Ag@Au-Ce6 NPs (Fig. 2C and D). In contrast, the fluorescence intensity changed slightly in PBS solu-
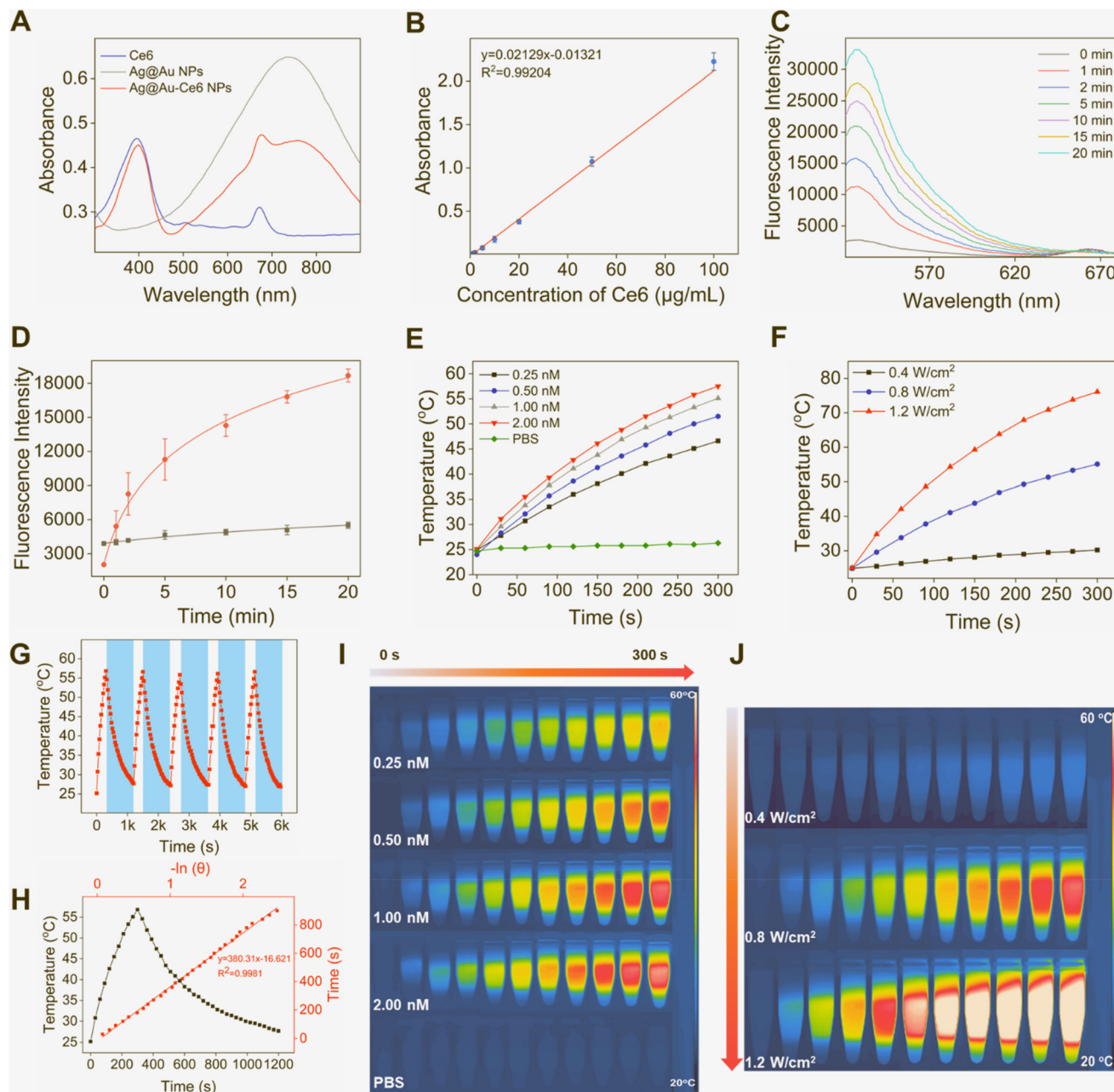
Fig. 2 Photodynamic and photothermal properties of Ag@Au-Ce6 NPs. (A) UV-vis spectra of free Ce6, Ag@Au NPs and Ag@Au-Ce6 NPs. (B) The calibration curve of Ce6 processed from UV-vis absorption peak at 400 nm. (C) Fluorescence spectra of Ag@Au-Ce6 NPs processed with the SOSG probe with laser illumination within 20 min (E_x: 488 nm, E_m: 520−700 nm). (D) The fluorescence intensities at 528 nm of PBS and Ag@Au-Ce6 NPs after adding the SOSG probe after laser irradiation within 20 min. (E) Temperature variation of PBS and different concentration of Ag@Au-Ce6 NPs (0.25, 0.5, 1, 2 nM) under 808 nm laser (0.8 W cm^{-2}) irradiation for 5 min and the corresponding thermal images (I). (F) Heating curve of Ag@Au-Ce6 NPs (1 nM) with increasing laser power intensity (0.4, 0.8, 1.2 W cm^{-2}) of a 808 nm laser for 5 min and thermal images (J). (G) Five heating/cooling cycle curves of Ag@Au-Ce6 NPs (an 808 nm laser, 1 nM, 0.8 W cm^{-2}). (H) The photothermal effects of Ag@Au-Ce6 NPs (1 nM, 0.8 W cm^{-2}) in black and the corresponding linear regression curve in red between $-\ln(\theta)$ and time under 808 nm laser irradiation for 5 min and cooling time for 15 min.

tion without $^1O_2$. These results indicated that Ag@Au-Ce6 NPs exhibited excellent PDT properties and had the potential for PDT treatment.

The photothermal property of the Ag@Au-Ce6 NPs was attributed to the strong absorption in the near-infrared region.[24] The photothermal character of Ag@Au-Ce6 NPs was first verified using Ag@Au-Ce6 NPs at different concentrations. Ag@Au-Ce6 NPs (0.25, 0.5, 1, 2 nM) were exposed to the 808 nm laser for 5 min at a power of 0.8 W cm^{-2}. The temperature of Ag@Au-Ce6 NPs for each concentration reached 46.5, 51.5, 55.1, and 57.5 °C, respectively, while the temperature of PBS solution merely increased from 24.7 °C to 26.3 °C. In

addition, the laser power was carefully controlled to evaluate the photothermal conversion properties. Different laser powers of 0.4, 0.8, and 1.2 W cm^{-2} were selected for Ag@Au-Ce6 NPs (1 nM) for 5 min and the temperature was elevated to 30.2, 55.1, and 76.1 °C, respectively (Fig. 2F and H). The photothermal efficiency of Ag@Au-Ce6 NPs is calculated to be 33.2%, compared with the similar metal photothermal nanomaterials, which is higher than those of Au nanoflowers (16.4%) and Au–Ag nanocages (31.2%), confirming that the alloy materials constructed in the work have achieved consistent or better photothermal conversion efficiency.[25,26] The calculation details are listed in the ESI.†

To check the photothermal stability of Ag@Au-Ce6 NPs, the heating–cooling cycle test was performed through 808 nm laser irradiation time of 5 min and a cooling time of 15 min (Fig. 2G). The temperature of Ag@Au-Ce6 NPs could almost recover the initial temperature even after 5 cycles. The thermal images of Ag@Au-Ce6 NPs at different concentrations and various laser power were recorded using an infrared thermal imager as shown in Fig. 2I and J, respectively. The above results demonstrated that the proposed Ag@Au-Ce6 NPs exhibited excellent photothermal conversion efficiency and stability, providing favorable conditions for subsequent experiments on the inhibition of bacterial growth by photothermal performance.

3.3 *In vitro* antibacterial efficiency

With the excellent photodynamic and photothermal properties, the antibacterial activity in bacterial culture *in vitro* was further confirmed by using Ag@Au-Ce6 NPs under 808 nm and 660 nm laser irradiation. *S. aureus* and *E. coli* were selected as model strains representing Gram-positive and Gram-negative bacteria, which induced serious bacterial infection.[27] Antibacterial materials are usually limited to the dense structure of Gram-negative bacteria due to the presence of the extracellular membrane layer.[28] Therefore, the loading concentration of Ce6 was set to 1 μM for *S. aureus* and 15 μM for *E. coli*, which was determined according to the encapsulation efficiency. First of all, the minimum inhibitory concentration was ascertained by means of the modified broth dilution method. The different concentrations of Ag@Au-Ce6 NPs (0.5, 0.25, 0.125, and 0.0625 nM) mixed with the bacterial solution in 96-well plates and irradiated by an 808 nm and a 660 nm laser. Thereafter, the mixture of Ag@Au-Ce6 NPs and bacteria was transferred to the LB broth medium and statically incubated for 24 h. The LB broth medium was regarded as the blank control, and the bacterial solution without any treatment was used as the negative control. The minimum concentration without visible turbidity was regarded as the minimum inhibitory concentration under the selected bacterial concentration.[29] As illustrated in Fig. 3A, when the concentration of Ag@Au-Ce6 NPs was as low as 0.25 nM, no obvious turbidity could be observed in the *S. aureus* group and the *E. coli* group. Consequently, the minimum inhibitory concentration was determined to be 0.25 nM, which was also used to discuss the antibacterial performance in the subsequent experiments.

In addition, the live/dead bacterial staining kit was employed to directly observe the antibacterial effect. The green fluorescence of SYTO 9 is considered as living bacteria with intact cell membranes, red fluorescence of PI showed dead bacteria with seriously impaired cell membranes.[30] The bacterial staining results obtained by CLSM exhibited that there was no obvious red fluorescence in the PBS group before and after laser irradiation. Furthermore, the CLSM images in the non-laser irradiation group treated with Ag@Au-Ce6 NPs had no apparent red fluorescence, implying that little damage occurred to bacteria. In contrast, the red fluorescence of *S. aureus* and *E. coli* significantly increased in the laser treatment group of Ag@Au-Ce6 NPs, and the green fluorescence decayed, suggesting that photodynamic–photothermal effect caused damage and death of a large number of bacterial membranes.

For the purpose of verifying the synergistic effect of PTT and PDT of Ag@Au-Ce6 NPs, the colony formation assay was performed under different treatments. As shown in Fig. 3C, the survival rates of *S. aureus* were 51.7% and 28.8% when Ag@Au NPs and Ce6 were used alone for photothermal or photodynamic inhibition, respectively, while the survival rates of *E. coli* treated with photothermal or photodynamic therapy alone were 49.4% and 60.1%, respectively. However, the inhibition rates toward *S. aureus* and *E. coli* reached approximately 100% after photothermal and photodynamic synergistic therapy using Ag@Au-Ce6 NPs. These results revealed that both the photothermal effect of nanoparticles and singlet oxygen generation by the loaded Ce6 could cause the antibacterial effect, furthermore, the synergistic PTT and PDT exhibited better antibacterial efficiency. Meanwhile, the bacterial colony count decreased slightly in the laser-irradiated PBS group and the laser-free Ag@Au-Ce6 NP group. Moreover, the sensitivity of *E. coli* to PDT was not as good as that of *S. aureus*, which might be related to the special outer membrane structure on the surface of Gram-negative bacteria that prevented $^1O_2$ from entering bacteria.[31,32]

Almost 80% of bacterial infection is associated with the bacteria biofilm, which is not only more resistant to external stimulation and damage than planktonic bacteria, but also plays a significant role in the spread of bacterial infection.[33,34] Therefore, the inhibition of bacterial biofilm formation and the formed biofilm are two crucial aspects to explore the anti-biofilm efficacy.[35] Owing to the great value of the *S. aureus* biofilm in implant infection, the *S. aureus* biofilm was used as a model for research.[36] The inhibition of biofilm formation based on Ag@Au-Ce6 NPs was first investigated. Crystal violet staining was used for the detection of biofilm removal. As demonstrated in Fig. 3F and H, biofilm formation was significantly reduced after irradiation for 5 min using an 808 nm and a 660 nm laser, respectively. These results not only inhibited the bacterial growth and biofilm formation of Ag@Au-Ce6 NPs under laser irradiation, but also validated the rationality of the laser irradiation time mentioned above.

As the formed biofilm could endure stronger exogenous stimuli, the inhibition of Ag@Au-Ce6 NPs toward the formed
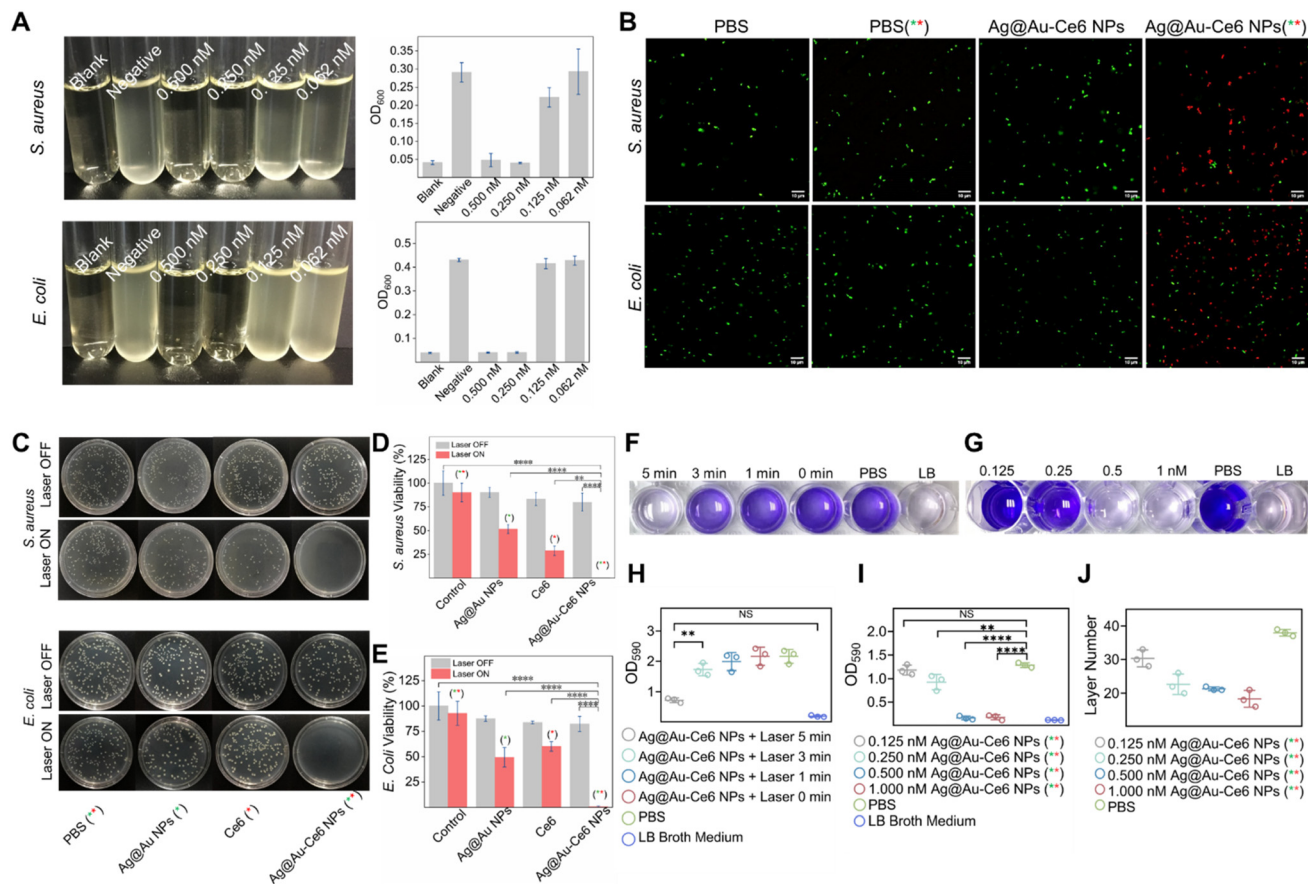
Fig. 3 *In vitro* antibacterial efficiency of Ag@Au-Ce6 NPs. (A) Photographs of *S. aureus* and *E. coli* cultured overnight in the LB broth medium after different treatments: blank, negative, Ag@Au-Ce6 NPs + laser (0.5, 0.25, 0.125, and 0.0625 nM) from left to right. The OD_{600} values of the corresponding culture products are shown. (B) Representative CLSM images of live/dead bacterial staining detection with PBS and Ag@Au-Ce6 treatment with or without laser irradiation (808 nm, 5 min + 660 nm, 5 min) of *S. aureus* and *E. coli* (green: SYTO 9, E_x: 488 nm, E_m: 510 nm−550 nm; red: PI, E_x: 561 nm, E_m: 617 nm−667 nm). Scale bar: 10 μm. (C) Colony formation images of *S. aureus* and *E. coli* after treatment with PBS, Ag NPs, Ce6, Ag@Au-Ce6, PBS (808 nm, 5 min + 660 nm, 5 min), Ag NPs (808 nm, 5 min), Ce6 (660 nm, 5 min), Ag@Au-Ce6 (808 nm, 5 min + 660 nm, 5 min) and the corresponding bacterial viability is measured in (D) and (E). (F) Photographs of biofilms formed in 24-well plates with crystal violet staining after various treatments: Ag@Au-Ce6 + laser (5, 3, 1, 0 min), PBS and LB broth medium. Quantitative analysis OD_{590} of crystal violet staining represented in (G). (H) Photographs of biofilms formed in 96-well plates with crystal violet staining after various treatments: Ag@Au-Ce6 + laser (0.125, 0.25, 0.5, and 1 nM), PBS and LB broth medium. Quantitative analysis of crystal violet staining represented in (I). (J) The layer counts of the final formed *S. aureus* biofilm (*n* = 3) under the treatment of Ag@Au-Ce6 + laser (0.125, 0.25, 0.5, and 1 nM), PBS and LB broth medium. The green * represents the groups subjected to 808 nm laser irradiation, 0.8 W cm^{-2} for 5 min. The red * means the groups treated with a 660 nm laser, 0.2 W cm^{-2} for 5 min. *P*-Value (*: <0.05, **: <0.01, ***: <0.001, ****: <0.0001).

biofilm was additionally investigated using the established *S. aureus* biofilm model. Crystal violet staining showed apparent differences among the finally formed biofilm samples after synergistic photothermal and photodynamic treatment (Fig. 3G and I). When the concentration of Ag@Au-Ce6 NPs was 0.5 nM, the growth of bacteria in the biofilm was significantly inhibited. In addition, the layer counts of the final formed *S. aureus* biofilm under different treatments were checked using CLSM after SYTO 9 staining (Fig. S1†). From the *Z*-axis scanning results of the biofilm, the thickness of the biofilm treated with 0.5 nM Ag@Au-Ce6 NPs was significantly thinner than the negative control group that was only treated with PBS, which also proved the great potential of Ag@Au-Ce6 NPs against the biofilm.

3.4 Investigation of the antibacterial mechanism

In order to further investigate the antibacterial mechanism of Ag@Au-Ce6 NPs, investigation experiments were carried out in the following three directions.

DCFH-DA is a versatile fluorescent probe that indicates the production of ROS.[37] Due to the presence of esterase, the DCFH-DA entering the cell is converted into DCFH. When encountering reactive oxygen species, fluorescent DCF can be generated from DCFH. Therefore, the fluorescence generation of DCF is detected to indicate the intracellular ROS concentration. In the typical confocal fluorescence images, it was found that there was no evident fluorescence signal inside the bacteria in the PBS control group, the PBS with laser

irradiation group, and the Ag@Au-Ce6 NPs without laser irradiation group (Fig. 4A). After the treatment of Ag@Au-Ce6 NPs combined with laser irradiation, obvious green fluorescence was emitted in *S. aureus* and *E. coli*, indicating a large number of ROS produced inside the bacteria. It could be inferred that the photothermal and photodynamic synergistic effect caused excessive ROS inside the bacteria, which burst out and overwhelmed the internal organelles, leading to the decline of the survival ability of the bacteria and eventually death.[38]

In order to identify the leakage of nucleic acid inside bacteria, OD_{260} value was used as an indicator to characterize the presence of DNA and RNA as indicated in Fig. 4B and C. Compared with the single photothermal or photodynamic treatment, the amount of nucleic acid released from the cells under the synergistic treatment showed a significant difference. Combined with the previous PI staining results, the permeability of the bacterial cell membrane changed in the course of treatment, leading to the dissociation of the cell contents from the damaged cell membrane.

In addition, we examined the membrane potential changes of the two experimental bacteria with the DiSC3(5) membrane potential probe. The fluorescence intensity increased sharply when the 0.5% Triton solution was added to the bacterial solution.[39] However, the fluorescence intensity decreased when Ag@Au-Ce6 NPs were added, and decreased more after laser irradiation, which revealed that the effect of Ag@Au-Ce6 NPs on bacterial membrane potential was caused by hyperpolarization in the process of synergistic photothermal and photodynamic effect rather than depolarization.[40] The hyperpolarization of the bacterial membrane may be caused by potassium efflux or tyrosine kinase-A (TrkA) inactivation, affecting ionic changes and eventually leading to membrane damage.[41]

TEM and SEM images were utilized to observe and compare the surface and internal structural changes of the bacteria after different treatments. As shown in Fig. 4F, the distribution of bacterial cytoplasm under 808 nm or 660 nm laser exposure was inhomogeneous, which was much different from the uniform and integrated content in the PBS group. However, under the photothermal and photodynamic synergistic therapy, the cell membrane was severely damaged or even completely destroyed and the cytoplasmic content generated qualitative changes. In the SEM images, the bacteria in PBS group displayed smooth appearance and uniform shape, while the cell membrane was deformed, shrunk or destroyed seriously in the synergistic photothermal–photodynamic groups. The abnormality of the bacterial morphology appeared to be more serious than that of photothermal or photodynamic treatment alone. In general, the changes of the surface cell membrane and cytoplasmic content properties were observed from TEM and SEM images. It was suggested that the changes of surface structure and internal cell contents were attributed to photothermal and photodynamic treatment, which induced cracking of the cell membrane and caused leakage of the cytoplasmic contents.

Based on the analysis of the above results based on the internal reactive oxygen species, cell content leakage of bacteria, membrane potential, and membrane morphology, it was rational to speculate that the antibacterial effect of photothermal and photodynamic therapy was caused by the thermal and chemical energy generation, leading to the destruction of the cell membrane structural integrity, the explosion of ROS inside the bacteria, and the hyperpolarization of the membrane potential. The internal proteins and other functional organelles were directly subjected to oxidative stress. Ultimately, the intracellular contents were released through the damaged cell membrane, promoting the loss of bacterial function and even bacterial death.

3.5 *In vivo* antibacterial efficiency

In order to further investigate the antibacterial application of Ag@Au-Ce6 NPs *in vivo*, the mouse wound infection model was constructed as demonstrated in Fig. 5A. A round wound with a diameter of 8 mm was constructed on the right posterior back of a female Balb/c mouse (18–22 g). Throughout the experiment, the wound scopes of the mice were recorded every other day and the area was calculated using Image J software. In the *S. aureus* group, it was observed that the healing rate of the blank group (without any bacterial inoculation) was consistently better than the others, and the other groups with higher healing rates were the Ag@Au-Ce6 NPs + laser group, Ag@Au NPs + laser group, and Ce6 + laser group, respectively. Compared with the PBS group and Ag@Au-Ce6 NPs without laser irradiation group, the Ag@Au-Ce6 NPs + laser group showed a better wound healing rate. And there was a similar trend in the experimental group of *E. coli*. Besides, the bacterial CFU of the wound samples at day 8 was counted for further analysis. The number of colonies in the Ag@Au-Ce6 NPs + laser group was significantly reduced, and that in the Ag@Au NPs + laser group (photothermal group) or the Ce6 + laser group (photodynamic group) was also decreased. However, in the PBS group and Ag@Au-Ce6 NPs without laser irradiation group, the colony counts were still high. Similar results could be found in the *E. coli* infection group. Compared to the photothermal or photodynamic therapy alone, photothermal and photodynamic synergistic therapy could significantly reduce the number of bacterial colonies and achieve a better wound healing outcome.

We next performed staining analysis of wounded skin collected on day 8 (Fig. 6). In the hematoxylin–eosin (HE) staining diagram, a large number of inflammatory cells were observed in the PBS group and Ag@Au-Ce6 NP group, while the number of inflammatory cells was less in the Ag@Au-Ce6 NPs + laser group, indicating that the number of bacteria was reduced and inflammatory infection was alleviated after Ag@Au-Ce6 NPs + laser treatment. Masson staining showed the formation of collagen fibers in blue. Under the synergistic effect of photothermal and photodynamic therapy, the blue collagen fibers were pervasive. In contrast, among the PBS group and the Ag@Au-Ce6 NP group, due to the residue of large numbers of bacteria, the wound was still in the stage of inflammatory infection to combat the bacteria. As a consequence, the wound recovered poorly and the formation of collagen fibers was less. More new
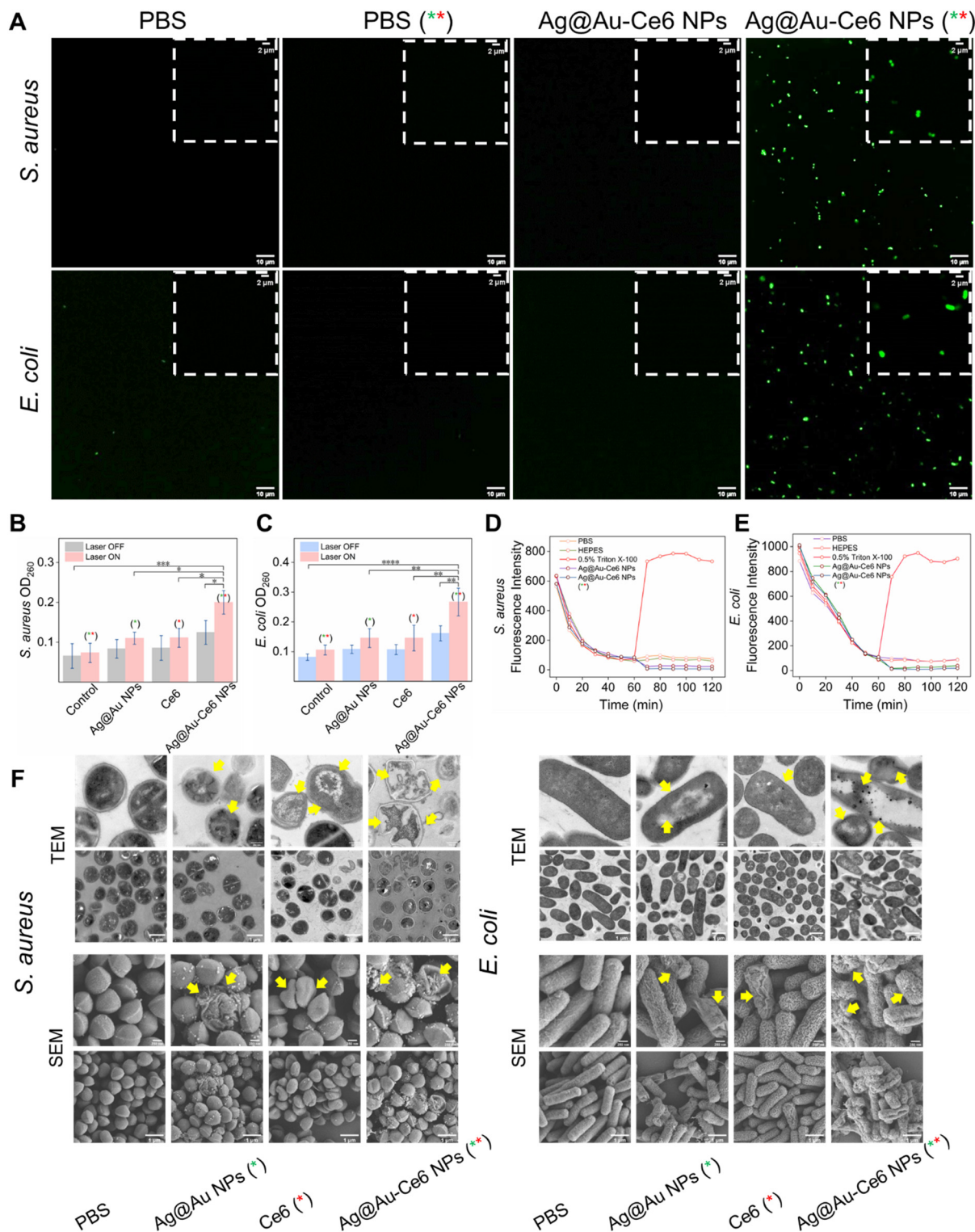
Fig. 4 Investigation on the antibacterial mechanism. (A) Representative CLSM images of DCFH-DA staining (E_x: 488 nm, E_m: 520–550 nm) of *S. aureus* and *E. coli* cultured with PBS and Ag@Au-Ce6 with or without laser irradiation (808 nm, 5 min + 660 nm, 5 min), scale bar: 10 μm. The insert figures show the locally enlarged fluorescent images, scale bar: 2 μm. OD_{260} value for the evaluation of the internal nucleic acid leakage from *S. aureus* (B) and *E. coli* (C) under different treatments: PBS, Ag NPs, Ce6, Ag@Au-Ce6 NPs, PBS (808 nm, 5 min + 660 nm, 5 min), Ag NPs (808 nm, 5 min), Ce6 (660 nm, 5 min), and Ag@Au-Ce6 NPs (808 nm, 5 min + 660 nm, 5 min). Fluorescence intensity changes of the DiSC3(5) probe after incubation with *S. aureus* (D) and *E. coli* (E) by different treatments: PBS, HEPES, 0.5% Triton, Ag@Au-Ce6 NPs and Ag@Au-Ce6 NPs (+laser). (F) The TEM and SEM images of *S. aureus* and *E. coli*, subjected to PBS, Ag NPs, Ce6, Ag@Au-Ce6 NPs, PBS (808 nm, 5 min + 660 nm, 5 min), Ag NPs (808 nm, 5 min), Ce6 (660 nm, 5 min), and Ag@Au-Ce6 NPs (808 nm, 5 min + 660 nm, 5 min) treatments. The green * represents the groups subjected to 808 nm laser irradiation, 0.8 W cm^{-2} for 5 min. The red * means the groups treated with a 660 nm laser, 0.2 W cm^{-2} for 5 min. Scale bar: 200 nm (upper), 1 μm (lower).
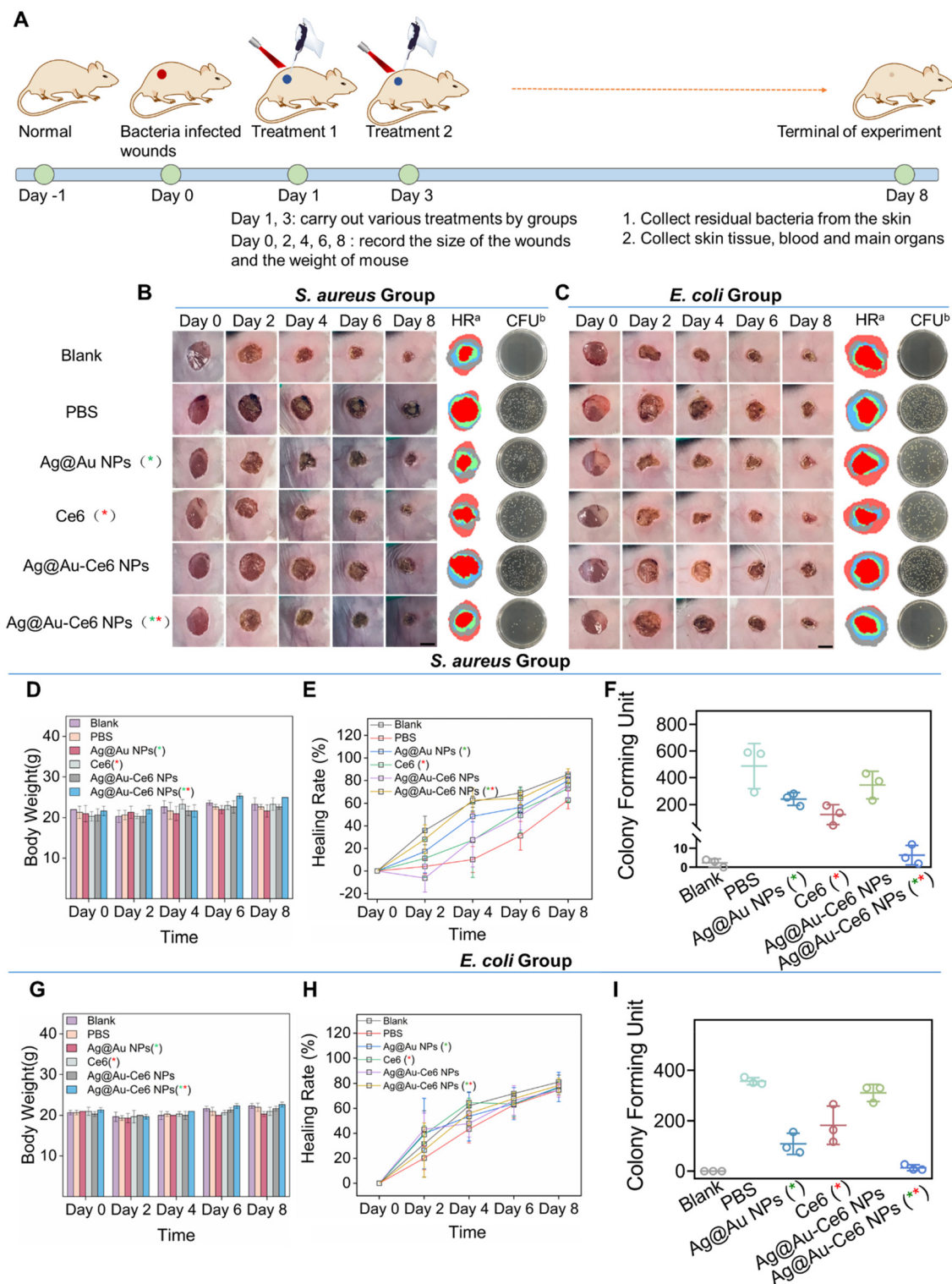
Fig. 5 *In vivo* antibacterial efficiency of Ag@Au-Ce6 NPs. (A) Schematic illustration of the establishment of wound infection mouse model and the overall experimental process. The blank group: no bacterium inoculation, the other groups inoculated with *S. aureus* (B) and *E. coli* (C). Representative wound pictures, simulation images of healing rates, and colony formation plates after different treatments (blank, PBS, Ag NPs (808 nm, 5 min), Ce6 (660 nm, 5 min), Ag@Au-Ce6 NPs, and Ag@Au-Ce6 NPs (808 nm, 5 min + 660 nm, 5 min)) in the wound model. The quantitative results of body weight, healing rate and plate colony forming unit counts of the mice model with *S. aureus* (D, E and F) and *E. coli* (G, H and I), respectively. The green * represents the groups subjected to 808 nm laser irradiation, 0.8 W cm^{-2} for 5 min. The red * means the groups treated with a 660 nm laser, 0.2 W cm^{-2} for 5 min.
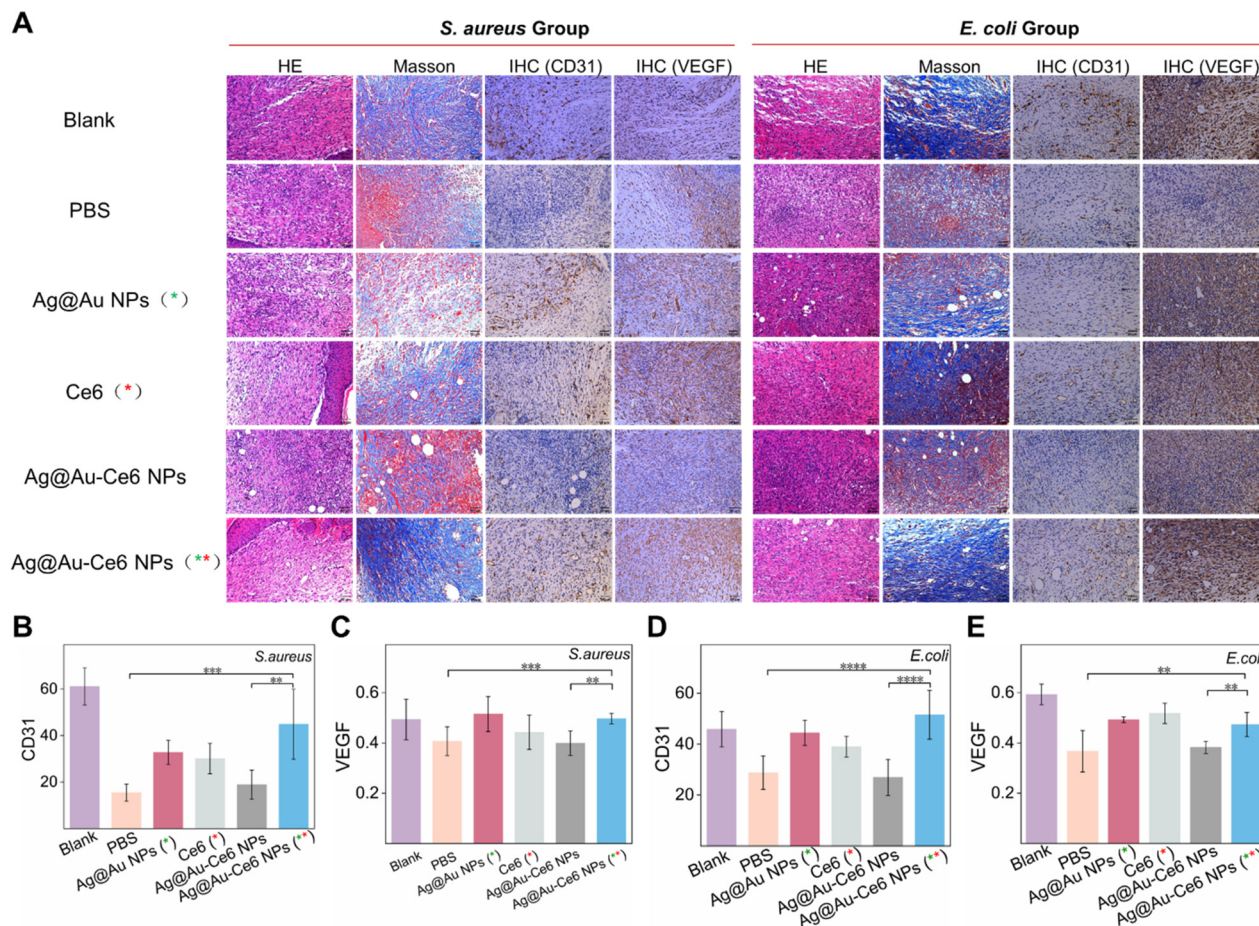
Fig. 6 Analysis of staining results for wound healing. (A) The HE staining, Masson's trichrome staining, and IHC staining of CD31, VEGF of mice skin wounds on day 8 after different treatments, scale bar: 50 μm. The immunohistochemical results of *S. aureus* infected mice included the number of blood vessels as shown by CD31 (B) and the mean optical density as shown by VEGF (C). While the immunohistochemical results of the *E. coli* group are shown in D (CD31) and E (VEGF). The green * represents the groups subjected to 808 nm laser irradiation, 0.8 W cm^{-2} for 5 min. The red * means the groups treated with a 660 nm laser, 0.2 W cm^{-2} for 5 min. *P*-value (*: <0.05, **: <0.01, ***: <0.001, ****: <0.0001).

granulation tissue formation was observed in the Ag@Au-Ce6 NPs + laser group. Platelet-endothelial cell adhesion molecules (CD31) as the specific marker of vascular endothelial cells, can be used to evaluate angiogenesis.[42] It could be found that the number of brown dark stained blood vessels representing CD31 (+) in the Ag@Au-Ce6 NPs + laser group was remarkably more than that in the PBS group and the Ag@Au-Ce6 NP group (Fig. 6B and D). As an important pro-vascular endothelial cell growth factor, VEGF also plays an extremely important role in angiogenesis.[43] IHC results exhibited that the average optical density value of VEGF in the Ag@Au-Ce6 NPs + laser group was stronger than that in the PBS group and the Ag@Au-Ce6 NP group, which suggested that photothermal and photodynamic synergistic therapy could effectively restrain the survival of bacteria and contribute to the formation of blood vessels during the wound healing process (Fig. 6C and E). Meanwhile, the normal angiogenesis of the surrounding skin also implied that the photothermal/photodynamic disinfection did not cause substantive damage to the surrounding skin. These results provided an important reference for clarifying

the effect of photothermal and photodynamic synergistic therapy on the outcome of inflammation and wound healing.

3.6 Biocompatibility evaluation

To evaluate the biocompatibility of Ag@Au-Ce6 NPs *in vitro*, a cytotoxicity assay, as well as the hemolysis assay, was performed. The survival rate of cells treated with Ag@Au-Ce6 NPs was quantified by the cell counting kit-8 method. With the increase of the used concentration of Ag@Au-Ce6 NPs, the cell survival rate decreased slightly (Fig. S2†). When the concentration was 2 nM, the survival rate of HACAT, NIH-3T3, and HUVEC cells could still be maintained above 80%, therefore it was considered to be biocompatible.

For the purpose of directly verifying the applicability of Ag@Au-Ce6 NPs within blood cells, blood samples were collected from Balb/c mice for hemolysis tests. The results are exhibited in Fig. S3.† Compared with the extremely severe hemolysis of the positive control Triton-X, no obvious hemolysis (hemolysis rate ≤5%) could be observed in the supernatant of other groups. Therefore, we possessed enough evidence to
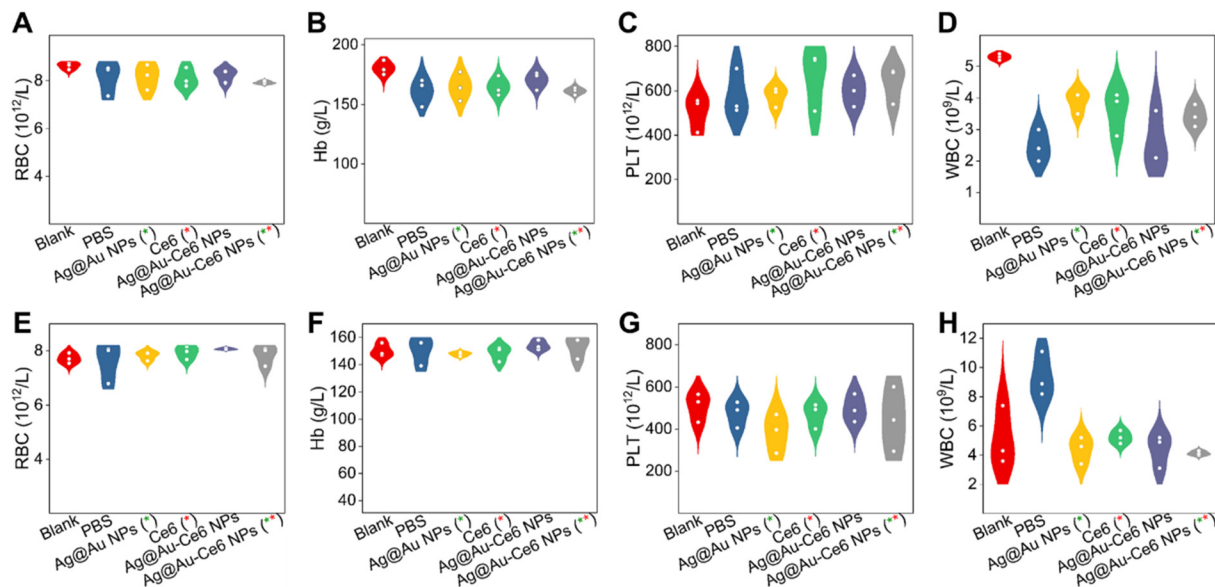
Fig. 7 Biosafety assessment of mice model with different treatments. The blood routine results of mice groups of *S. aureus* (A– D) and *E. coli* (E–H) with various treatments. The green * represents the groups subjected to 808 nm laser irradiation, 0.8 W cm^{-2} for 5 min. The red * means the groups treated with a 660 nm laser, 0.2 W cm^{-2} for 5 min.

believe that the toxicity of Ag@Au-Ce6 NPs to blood cells was within the tolerable range of organisms, and could be applied in biological experiments.

In order to further evaluate the cytotoxicity of Ag@Au-Ce6 NPs *in vivo*, we focused on the body weight, routine blood test, and pathological structural examination of the main organs of mice. During the experiment, although the weight of the mice showed a weight loss trend on the second day, the weight gradually recovered in the later period, with no obvious difference between different groups. The blood routine analysis of red blood cells (RBCs), hemoglobin (Hb), platelets (PLTs), and white blood cells (WBCs) of the mice on the eighth day had no clear difference in the six groups. Consistent with the low hemolysis rate results described above, Ag@Au-Ce6 NPs showed excellent biocompatibility (Fig. 7). Finally, the main organs of the mice were inspected and stained. The results revealed that there was no obvious pathological abnormality on the surface of these gross organs, and the histological analysis results showed that the nanoparticles could hardly cause noticeable changes to the heart, liver, spleen, lungs, and kidneys (Fig. S4†). These results indicated that the Ag@Au-Ce6 NPs had good biocompatibility *in vivo* and were friendly for biological experiments, and could be utilized for more experimental exploration *in vivo*.

The experimental results verified that the hollow silver–gold alloy nanoparticles had great achievements as an antibacterial agent, promoting skin wound healing. It is believed that the constructed synergistic antibacterial nanomaterials will also have strong potential for the treatment of drug-resistant bacteria. Although a lot of experimental results have been obtained in this work, there are still many shortcomings in the experimental system that cannot be ignored. The shortcom-

ings and prospects can be listed as follows. (1) The construction of the whole system requires further improvement and innovation. On the one hand, the antibacterial and healing effects of the nanotherapeutic platform can be improved. On the other hand, it is necessary to increase the targeting and response release to the bacterial infection microenvironment for reducing the side impact on the surrounding healthy tissues. (2) Although a series of biocompatibility experiments have been carried out, the biosafety of metal nanoparticles in *in vivo* metabolism has not yet been fully and comprehensively considered. The degradability, thrombosis and aggregation changes of nanoparticles in the blood flow are worthy of further study for *in vivo* practical application. (3) The combined platform with multiple systems is beneficial for the optimization of the antibacterial effect and wound healing. For example, the combined application of a hydrogel can protect the wound from pollution and retain the effective ingredients of drugs, achieving better therapeutic effect through slow release, moreover, it can avoid multiple risks caused by repeated addition of drugs.[44,45]

4. Conclusions

In summary, hollow silver–gold alloy nanoparticles immobilized with the photosensitizer molecule Ce6 were successfully developed as synergistic PTT/PDT nanoagents to kill bacteria and accelerate wound healing of infected skin. Hollow Ag@Au alloy NPs exhibited satisfactory PTT performance with mild hyperthermia, which decreased the damage to the surrounding healthy tissues. After immobilizing with Ce6 molecules on the surface of Ag@Au alloy NPs, the nanosystem of PTT

integrated PDT was fabricated and it eliminated *S. aureus* and *E. coli* infection by mild hyperthermia and ROS generation, synchronously promoting epithelium migration and vascularization. As a proof-of-concept, the nanoagents achieved favourable performance in the healing process of bacteria-infected wounds, which may facilitate the clinical translation of synergistic PTT/PDT treatment for wounded skin.

Conflicts of interest

There are no conflicts to declare.

Acknowledgements

References

1 D. I. Andersson and D. Hughes, *Nat. Rev. Microbiol.*, 2010, **8**, 260–271.

2 M. Xue, R. Zhao, H. Lin and C. Jackson, *Adv. Drug Delivery Rev.*, 2018, **129**, 219–241.

3 J. S. Chin, L. Madden, S. Y. Chew and D. L. Becker, *Adv. Drug Delivery Rev.*, 2019, **149–150**, 2–18.

4 D. M. Morens, G. K. Folkers and A. S. Fauci, *Nature*, 2004, **430**, 242–249.

5 H. C. Flemming, J. Wingender, U. Szewzyk, P. Steinberg, S. A. Rice and S. Kjelleberg, *Nat. Rev. Microbiol.*, 2016, **14**, 563–575.

6 F. D. Lowy, *N. Engl. J. Med.*, 1998, **339**, 520–532.

7 J. Huo, Q. Jia, H. Huang, J. Zhang, P. Li, X. Dong and W. Huang, *Chem. Soc. Rev.*, 2021, **50**, 8762–8789.

8 J. M. V. Makabenta, A. Nabawy, C.-H. Li, S. Schmidt-Malan, R. Patel and V. M. Rotello, *Nat. Rev. Microbiol.*, 2021, **19**, 23–36.

9 M. J. Hajipour, K. M. Fromm, A. A. Ashkarran, D. Jimenez de Aberasturi, I. R. de Larramendi, T. Rojo, V. Serpooshan, W. J. Parak and M. Mahmoudi, *Trends Biotechnol.*, 2012, **30**, 499–511.

10 X. Li, S. Lee and J. Yoon, *Chem. Soc. Rev.*, 2018, **47**, 1174–1188.

11 S. Hao, H. Han, Z. Yang, M. Chen, Y. Jiang, G. Lu, L. Dong, H. Wen, H. Li, J. Liu, L. Wu, Z. Wang and F. Wang, *Nano-Micro Lett.*, 2022, **14**, 178.

12 W. Fan, P. Huang and X. Chen, *Chem. Soc. Rev.*, 2016, **45**, 6488–6519.

13 Q. Zheng, X. Liu, Y. Zheng, K. W. K. Yeung, Z. Cui, Y. Liang, Z. Li, S. Zhu, X. Wang and S. Wu, *Chem. Soc. Rev.*, 2021, **50**, 5086–5125.

14 C. Xu and K. Pu, *Chem. Soc. Rev.*, 2021, **50**, 1111–1137.

15 C. Mao, Y. Xiang, X. Liu, Z. Cui, X. Yang, Z. Li, S. Zhu, Y. Zheng, K. W. K. Yeung and S. Wu, *ACS Nano*, 2018, **12**, 1747–1759.

16 A. El-Kenawi and B. Ruffell, *Cancer Cell*, 2017, **32**, 727–729.

17 Z. Yuan, C. Lin, Y. He, B. Tao, M. Chen, J. Zhang, P. Liu and K. Cai, *ACS Nano*, 2020, **14**, 3546–3562.

18 J. He, Z. Zhang, Y. Yang, F. Ren, J. Li, S. Zhu, F. Ma, R. Wu, Y. Lv, G. He, B. Guo and D. Chu, *Nano-Micro Lett.*, 2021, **13**, 80.

19 A. Maleki, J. He, S. Bochani, V. Nosrati, M. A. Shahbazi and B. Guo, *ACS Nano*, 2021, **15**, 18895–18930.

20 B. Chen, X. Jiao and D. Chen, *Cryst. Growth Des.*, 2010, **10**, 3378–3386.

21 K. Wu, H. Zhao, Z. Sun, B. Wang, X. Tang, Y. Dai, M. Li, Q. Shen, H. Zhang, Q. Fan and W. Huang, *Theranostics*, 2019, **9**, 7697–7713.

22 S. E. Skrabalak, L. Au, X. Li and Y. Xia, *Nat. Protoc.*, 2007, **2**, 2182–2190.

23 A. Lin, Y. Liu, X. Zhu, X. Chen, J. Liu, Y. Zhou, X. Qin and J. Liu, *ACS Nano*, 2019, **13**, 13965–13984.

24 L. E. Theune, J. Buchmann, S. Wedepohl, M. Molina, J. Laufer and M. Calderón, *J. Controlled Release*, 2019, **311–312**, 147–161.

25 F. Wu, Y. Liu, Y. Wu, D. Song, J. Qian and B. Zhu, *J. Mater. Chem. B*, 2020, **8**, 2128–2138.

26 T. Jiang, J. Song, W. Zhang, H. Wang, X. Li, R. Xia, L. Zhu and X. Xu, *ACS Appl. Mater. Interfaces*, 2015, **7**, 21985–21994.

27 N. Woodford and D. M. Livermore, *J. Infect.*, 2009, **59**, S4–S16.

28 R. Wang, D. Kim, M. Yang, X. Li and J. Yoon, *ACS Appl. Mater. Interfaces*, 2022, **14**, 7609–7616.

29 I. O. Chikezie, *Afr. J. Microbiol. Res.*, 2017, **11**, 977–980.

30 X. Huang, Z. Zhang, L. Chen, Y. Lin, R. Zeng, J. Xu, S. Chen, J. Zhang, H. Cai, H. Zhou and P. Sun, *Biosens. Bioelectron.*, 2022, **212**, 114414.

31 H. Nikaido, *Science*, 1994, **264**, 382–388.

32 J. M. Blair, M. A. Webber, A. J. Baylay, D. O. Ogbolu and L. J. Piddock, *Nat. Rev. Microbiol.*, 2015, **13**, 42–51.

33 D. E. Moormeier and K. W. Bayles, *Mol. Microbiol.*, 2017, **104**, 365–376.

34 O. Ciofu, C. Moser, P. Ø. Jensen and N. Høiby, *Nat. Rev. Microbiol.*, 2022, **20**, 621–635.

35 Z. Liang, X. Wang, G. Yu, M. Li, S. Shi, H. Bao, C. Chen, D. Fu, W. Ma, C. Xue and B. Sun, *Nano Today*, 2022, **43**, 101445.

36 C. R. Arciola, D. Campoccia and L. Montanaro, *Nat. Rev. Microbiol.*, 2018, **16**, 397–409.

37 W. O. Carter, P. K. Narayanan and J. P. Robinson, *J. Leukocyte Biol.*, 1994, **55**, 253–258.

38 Z. Xu, C. Zhang, Y. Yu, W. Li, Z. Ma, J. Wang, X. Zhang, H. Gao and D. Liu, *Nanotheranostics*, 2021, **5**, 472–487.

39 M. Zhou, Y. Qian, J. Xie, W. Zhang, W. Jiang, X. Xiao, S. Chen, C. Dai, Z. Cong, Z. Ji, N. Shao, L. Liu, Y. Wu and R. Liu, *Angew. Chem., Int. Ed.*, 2020, **59**, 6412–6419.

40 L. Gao, J. Cheng, Z. Shen, G. Zhang, S. Liu and J. Hu, *Angew. Chem., Int. Ed.*, 2022, **61**, e202112782.

41 S. Oncul, E. M. Cuce, B. Aksu and A. Inhan-Garip, *Int. J. Radiat. Biol.*, 2016, **92**, 42–49.

42 Z. Guo, J. X. He, S. H. Mahadevegowda, S. H. Kho, M. B. Chan-Park and X. W. Liu, *Adv. Healthcare Mater.*, 2020, **9**, e2000265.

43 W. Li, S. Wang, D. Zhong, Z. Du and M. Zhou, *Adv. Ther.*, 2021, **4**, 2000107.

44 Y. Liang, H. Xu, Z. Li, A. Zhangji and B. Guo, *Nano-Micro Lett.*, 2022, **14**, 185.

45 Y. Huang, L. Mu, X. Zhao, Y. Han and B. Guo, *ACS Nano*, 2022, **16**, 13022–13036.